



# CHORUS

This is the accepted manuscript made available via CHORUS. The article has been published as:

## Dynamic polarizability measurements with $^{176}\text{Lu}^{\{+\}}$

K. J. Arnold, R. Kaewuam, T. R. Tan, S. G. Porsev, M. S. Safronova, and M. D. Barrett

Phys. Rev. A **99**, 012510 — Published 15 January 2019

DOI: [10.1103/PhysRevA.99.012510](https://doi.org/10.1103/PhysRevA.99.012510)

# Dynamic polarizability measurements in $^{176}\text{Lu}^+$

K. J. Arnold<sup>1,\*</sup>, R. Kaewuam<sup>1</sup>, T. R. Tan<sup>1,2</sup>, S. G. Porsev<sup>3,4</sup>, M. S. Safronova<sup>3,5</sup>, and M. D. Barrett<sup>1,2†</sup>

<sup>1</sup>*Centre for Quantum Technologies, 3 Science Drive 2, 117543 Singapore*

<sup>2</sup>*Department of Physics, National University of Singapore, 2 Science Drive 3, 117551 Singapore*

<sup>3</sup>*Department of Physics and Astronomy, University of Delaware, Newark, Delaware 19716, USA*

<sup>4</sup>*Petersburg Nuclear Physics Institute of NRC “Kurchatov Institute”, Gatchina, Leningrad District 188300, Russia*

<sup>5</sup>*Joint Quantum Institute, National Institute of Standards and Technology*

*and the University of Maryland, College Park, Maryland 20742, USA*

We measure the differential polarizability of the  $^{176}\text{Lu}^+ \ ^1S_0 \leftrightarrow \ ^3D_1$  clock transition at multiple wavelengths. This experimentally characterizes the differential dynamic polarizability for frequencies up to 372 THz and allows an experimental determination of the dynamic correction to the blackbody radiation shift for the clock transition. In addition, measurements at the near resonant wavelengths of 598 and 646 nm determine the two dominant contributions to the differential dynamic polarizability below 372 THz. These additional measurements are carried out by two independent methods to verify the validity of our methodology. We also carry out a theoretical calculation of the polarizabilities using the hybrid method that combines the configuration interaction (CI) and the coupled-cluster approaches, incorporating for the first time quadratic non-linear terms and partial triple excitations in the coupled-cluster calculations. The experimental measurements of the  $\langle \ ^3D_1 || r || \ ^3P_J \rangle$  matrix elements provide high-precision benchmarks for this theoretical approach.

PACS numbers: 06.30.Ft, 06.20.fb

The differential scalar polarizability,  $\Delta\alpha_0(\omega)$ , of a clock transition is an important quantity to determine. The dc value  $\Delta\alpha_0(0)$  quantifies the blackbody radiation (BBR) shift, and contributes to micromotion shift assessments in ion-based clocks. The variation of the polarizability over the BBR spectrum determines the so-called dynamic correction to the BBR shift [1], and the value at the clock frequency quantifies sensitivity to probe-induced ac Stark shifts.

For the  $^{176}\text{Lu}^+ \ ^1S_0 \leftrightarrow \ ^3D_1$  transition at 848 nm, the recent measurement of  $\Delta\alpha_0(\omega)$  at  $10.6 \mu\text{m}$  inferred an exceptionally small BBR shift of  $-1.36(9) \times 10^{-18}$  at 300 K [2]. As the measurement was carried out at a frequency that is fairly central to the BBR spectrum, the assessment is insensitive to the true dc value of  $\Delta\alpha_0(\omega)$  and its variation over the BBR spectrum. Nevertheless, it is still of interest to make an experimental assessment, as  $\Delta\alpha_0(0)$  can factor into planned assessments of the dc polarizability of the  $^1S_0 \leftrightarrow \ ^3D_2$  and  $^1S_0 \leftrightarrow \ ^1D_2$  clock transitions at 804 and 577 nm, respectively.

The accuracy of the BBR assessment for the 848-nm transition relies on the small measured value of  $\Delta\alpha_0(\omega)$  at  $10.6 \mu\text{m}$ ; a modest fractional error in a small number is still a small number. This is not the case for the other two clock transitions in  $^{176}\text{Lu}^+$ . For these two transitions micromotion-induced shifts can be used to determine  $\Delta\alpha_0(0)$  as done in [3]. For  $^{176}\text{Lu}^+$  this can be elegantly done by measuring frequency ratios within the same apparatus. In this case many systematics are common mode. The difference in the ratio with and without micromotion depends only on (a) the micromotion

amplitude, which can be accurately characterized from micromotion sidebands, and (b) the difference in  $\Delta\alpha_0(0)$  for the two transitions. Assessment of  $\Delta\alpha_0(0)$  for the 804- and 577-nm transitions by comparison to the 848-nm clock would then be limited by the small contribution from the 848-nm transition.

In light of the above considerations,  $\Delta\alpha_0(\omega)$  for the 848-nm transition has been measured at six optical frequencies corresponding to the approximate wavelengths 1560, 987, 848, 804, 646, and 598 nm. All measurements, together with previous measurements at  $10.6 \mu\text{m}$  [2], are then used to formulate a model for  $\Delta\alpha_0(\omega)$  for frequencies up to 372 THz (804 nm) providing an estimate of  $\Delta\alpha_0(0)$ , and a reassessment of the BBR shift.

Measurements at 598 and 646 nm determine the dominant pole contributions to  $\Delta\alpha_0(\omega)$  which largely determine the frequency dependence below 372 THz ( $\lambda = 804 \text{ nm}$ ). The 598 and 646 measurements are independently verified using an alternative technique based on the comparison of ac Stark shifts and scattering rates [4]. With this technique, the dependence on laser intensity factors out and provides a consistency check for the more conventional approach that involves characterizing the beam intensity [5, 6].

The paper is organized into three main sections. The first section details the experimental and theoretical methodologies, the measurements made, and compares theoretical and experimental results for the matrix elements and polarizabilities. The second section develops a suitable model for  $\Delta\alpha_0(\omega)$  based on a theoretical understanding of the atomic structure and supported by the measurements. An independent assessment based on the single pole approximation [6] is used for comparison as a means to check for modeling dependencies. The final section applies the results to the BBR assessment.

\* cqtjka@nus.edu.sg

† phybmd@nus.edu.sg

## I. POLARIZABILITY MEASUREMENTS

The experimental methodology employed is similar to that reported in previous work [2]. Linearly polarized light is focused on the ion to induce an ac Stark shift. This shift is measured on either the optical transition,  $|^1S_0, F=7, m_F=0\rangle \leftrightarrow |^3D_1, 7, 0\rangle$ , or the microwave transition  $|^3D_1, 7, 0\rangle \leftrightarrow |^3D_1, 6, 0\rangle$ . The optical transition is realized as an average of the  $|^1S_0, 7, \pm 1\rangle \leftrightarrow |^3D_1, 7, 0\rangle$  transitions probed by Rabi spectroscopy with typical  $\pi$ -times of 5–20 ms. The ac Stark shift is measured by an interleaved servo technique [2, 7]. The laser intensity is determined from *in situ* 2D profiling of the beam at the ion, and power measurements using a calibrated detector.

### A. Experimental setup and optical power characterization

Experiments are performed in the same linear Paul trap used for previous work [8]. The trap consists of two axial endcaps separated by 2 mm and four rods arranged on a square with sides 1.2 mm in length. All electrodes are made from 0.45 mm electropolished copper-beryllium rods. Radial confinement is provided by a 16.8 MHz radio-frequency (rf) potential applied to a pair of diagonally opposing electrodes via a helical quarter-wave resonator. A dc voltage applied to the other pair of diagonally opposing electrodes ensures a splitting of the transverse trapping frequencies. The endcaps are held at 8 V to provide axial confinement. The measured trap frequencies of a single  $\text{Lu}^+$  are  $(\omega_x, \omega_x, \omega_z) \approx 2\pi \times (608, 560, 134)$  kHz, with the trap axis along  $z$ .

The optical setup for the ac-Stark shift laser is shown schematically in Fig. 2. The light is delivered to the experiment on a single mode optical fiber. An assembly consisting of an aspheric lens to collimate the fiber output, a Glan-Taylor polarizer to set the polarization, and an achromat doublet to focus onto the ion, is mounted on a motorized two-axis translation stage which has specified bi-directional repeatability of  $1.5 \mu\text{m}$ . The exact optical components of this assembly are changed as needed to be suitable for the laser wavelength used (1560, 987, 848, 804, 646, or 598 nm). The reflection from the first surface of the fixed-position glass pick-off is captured by a charge-coupled device (CCD) to characterize the movement of the stage during beam profiling.

The first reflection from the vacuum viewport,  $P_2$  in Fig. 2, is used to actively stabilize the optical power by feedback onto an acousto-optic modulator (AOM) before the optical fiber. When the active stabilization is engaged, the reading on the monitor power meter at  $P_4$  is repeatable to the lowest significant display digit over a day, and measurements of the ac-Stark shift indicate fractional power instability less than  $10^{-3}$  as shown in Fig. 1. To determine the optical power at the ion,  $P_0$ , the vacuum viewport transmission,  $T = (P_1 - P_2 - P_3)/P_1$ ,

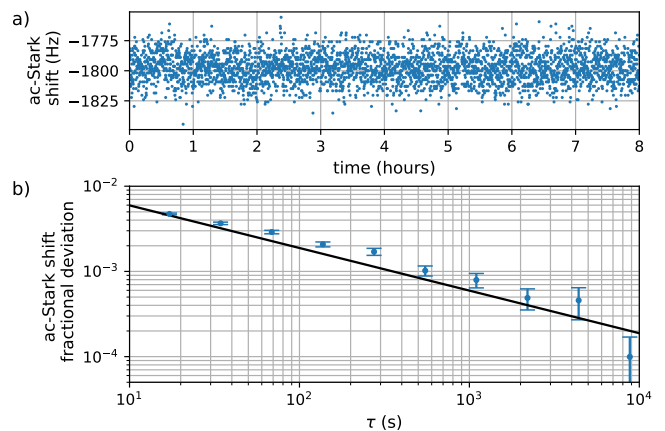


FIG. 1. (a) ac-Stark shift induced by an intensity-stabilized 646 nm laser which is measured for 8 hours by the interleaved servo technique. (b) Allan deviation of the data in (a) compared to the servo projection noise limit (black line).

and the ratio of reference and monitor detectors readings,  $r = P_{\text{ref}}/P_{\text{mon}}$ , are measured while the active stabilization is disengaged. The power at the ion with the stabilization engaged is then  $P_0 = rTP_4$ , with an uncertainty determined by the calibration accuracy of the reference detector and the statistical uncertainty in  $r$  and  $T$ . Two of our commercial detectors were calibrated by the National Metrology Centre (NMC) in Singapore: a Silicon-based detector at 633 and 850 nm, and Germanium-based detector at 976 and 1550 nm. All NMC calibrations have a certified  $2\sigma$  uncertainty of 1.5%. For each laser wavelength used in the experiment, the reference detector's calibration is traceable to the NMC calibration at the nearest wavelength.

### B. Beam profiling and intensity characterization

In order to determine the laser intensity, the beam is profiled by measuring the position-dependent ac Stark shift  $\delta f(x', y')$  induced on the  $|^1S_0, 7, 0\rangle \leftrightarrow |^3D_1, 7, 0\rangle$  clock transition as the beam is displaced by motorized translation stages (Fig. 2) in a two-dimensional space  $(x', y')$  orthogonal to the laser direction. We define a normalization constant

$$C = \frac{\delta f_{\text{max}}}{\iint \delta f(x', y') dx' dy'} \quad (1)$$

where  $\delta f_{\text{max}}$  is the peak ac Stark shift and  $C$  has units of  $\text{m}^{-2}$ . The peak beam intensity is then  $I_0 = CP_0$ . A useful length scale to parameterize the mode is the effective waist  $w_e = \sqrt{2/(\pi C)}$ , which corresponds to the waist of a Gaussian beam with the same normalization constant  $C$ .

After each movement of the translation stages, the beam center position is determined by a 2D Gaussian

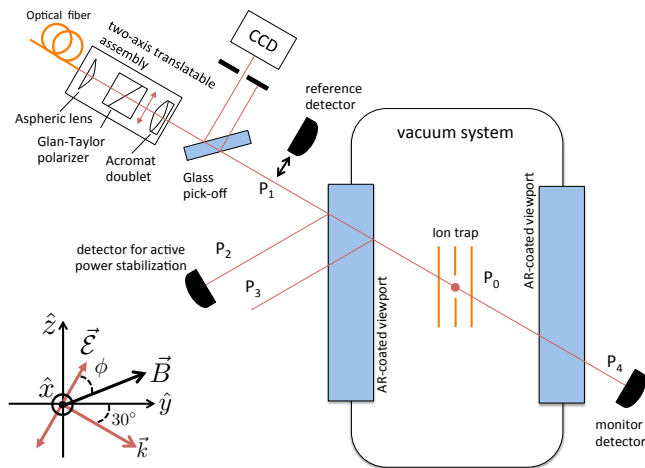


FIG. 2. (Color Online) Schematic of experimental setup. The light shifting laser is delivered to the experiment by optical fiber. The optics assembly to collimate and then focus the light onto the ion is able to be displaced along both axes orthogonal to the beam direction using motorized translation stages. A CCD camera monitors the beam displacement. Power measurement at the points  $P_1$  to  $P_4$  are used to infer the power at ion,  $P_0$ , as described in the main text. The laser direction  $\vec{k}$  is approximately  $30^\circ$  from normal incidence with respect to the viewport. The externally applied magnetic field  $\vec{B}$  is rotated in the  $yz$ -plane to form an angle  $\phi$  with respect to the linear laser polarization  $\vec{E}$ .

fit to an image captured by the fixed position CCD camera shown in Fig. 3. The beam position measurement by the CCD camera has  $\pm 150$  nm repeatability. Observed over the course more than 34 hours, the beam position is observed to drift by approximately  $3 \mu\text{m}$  over the course of one day, with maximum rate of  $9 \mu\text{m}/\text{day}$ , correlated with the ambient lab temperature. For a typical profile scan over a  $300 \mu\text{m}$  square grid, the rms positioning error of the stages relative to the programmed coordinates is  $\sim 1 \mu\text{m}$  as assessed by the CCD camera. The beam displacement measured by the camera at each point is used for position coordinates when evaluating the beam profiles.

The ac-Stark shift profile for the 598 nm laser is shown in Fig. 3a as a representative dataset. Here Rabi spectroscopy with a 9 ms  $\pi$ -time is used. The measurement at each position is the average value after 20 interleaved servo updates, where one update occurs after 160 interrogations alternately with and without the Stark shift beam present. Before starting each measurement, the servo is run for 5 iterations to lock onto the Stark-shifted line to avoid servo error in the averaged value. For the data in Fig. 3a, the peak Stark shift is -528.8 Hz and the projection noise limited uncertainty at each position is 1.0 Hz. The mode function is approximated by a cubic spline interpolation, and integration over the square data region yields a normalization constant of  $C = 117.1(3) \text{mm}^{-2}$ , corresponding to  $w_e = 73.73(9) \mu\text{m}$ . The statistical uncertainty of  $C$  is determined by a bootstrapping method

where new data is generated by a Monte Carlo method allowing for variation due to (i) the projection noise in each measurement, (ii) an overall position offset of the coordinates with respect to the measured profile, and (iii) beam pointing drift over the duration of the profile measurement. Three profiles were taken for both 646 and 804 nm and the repeatability was consistent with the uncertainty estimated by this method. For the other wavelengths, only a single profile was taken.

A potential source of systematic error with this methodology is beam power not captured within the data region. To illustrate, consider two test functions in Fig. 3(c-d) with the same normalization as our measured profile: a Gaussian (blue solid line) and Airy distribution (green dashed line) with respective intensity distributions

$$\frac{I(r)}{I_0} = e^{-\frac{2r^2}{w_e^2}} \quad \text{and} \quad \frac{1}{2} \left( \frac{w_e}{r} J_1 \left( \frac{r\sqrt{8}}{w_e} \right) \right)^2,$$

where  $J_1$  is the Bessel function of the first kind of order one. The Airy function, a realistic optical profile resulting from uniform illumination of a circular aperture, has a significant fraction of power distributed over regions of large  $r/w_e$ . Even a partial contribution of the Airy distribution to the laser profile, which could result from either beam clipping or focusing aberration, for example, would be undetectable within the projection noise at the tails of the measured profile, yet still result in significant error for a data region extending to  $r/w_e = 3.5$  (Fig. 3d). Considering the measured ac Stark shifts (dark orange points, Fig. 3c), even the modest deviation of the observed profile from a Gaussian at the tails of the distribution (inset Fig. 3c) requires the data region to be extended from  $r/w_e = 1.5$  to 2 in order to achieve 99% power capture (inset Fig. 3d).

For the last two wavelengths measured, 646 and 598 nm, the low-intensity tails of the distribution were further investigated by independently profiling the beam with a low readout noise camera outside of vacuum. With the same optical assembly used for the experiment (Fig. 2), including a glass pick-off and an identical vacuum viewport, beam profile images were captured at several positions around the focal plane. For 598 nm, the camera image which had normalization nearest ( $C = 118.8 \text{mm}^{-2}$ ) to the measured ac-Stark profile is shown in Fig. 3b. From the camera data (light orange points) in Fig. 3c, we see good agreement with the ac-Stark data within the profiled region ( $r/w_e < 3.5$ ) and no significant intensity beyond  $r/w_e > 3.5$ . For 598-nm, the camera data indicates the  $360 \mu\text{m}$  square grid used for the ac-Stark profile captures  $\gtrsim 99.8\%$  of the power.

For wavelengths 804, 848, and 987 nm, the beam had been profiled at the focus only for the purpose of estimating the beam waist, at that time. For assessing the fraction of power not captured within the scan region of the ac-Stark shift profile,  $P_{\text{loss}}$ , only the 987 nm camera profile was of sufficient quality to extract useful quantitative information at a later date. For 1560 nm, we did not

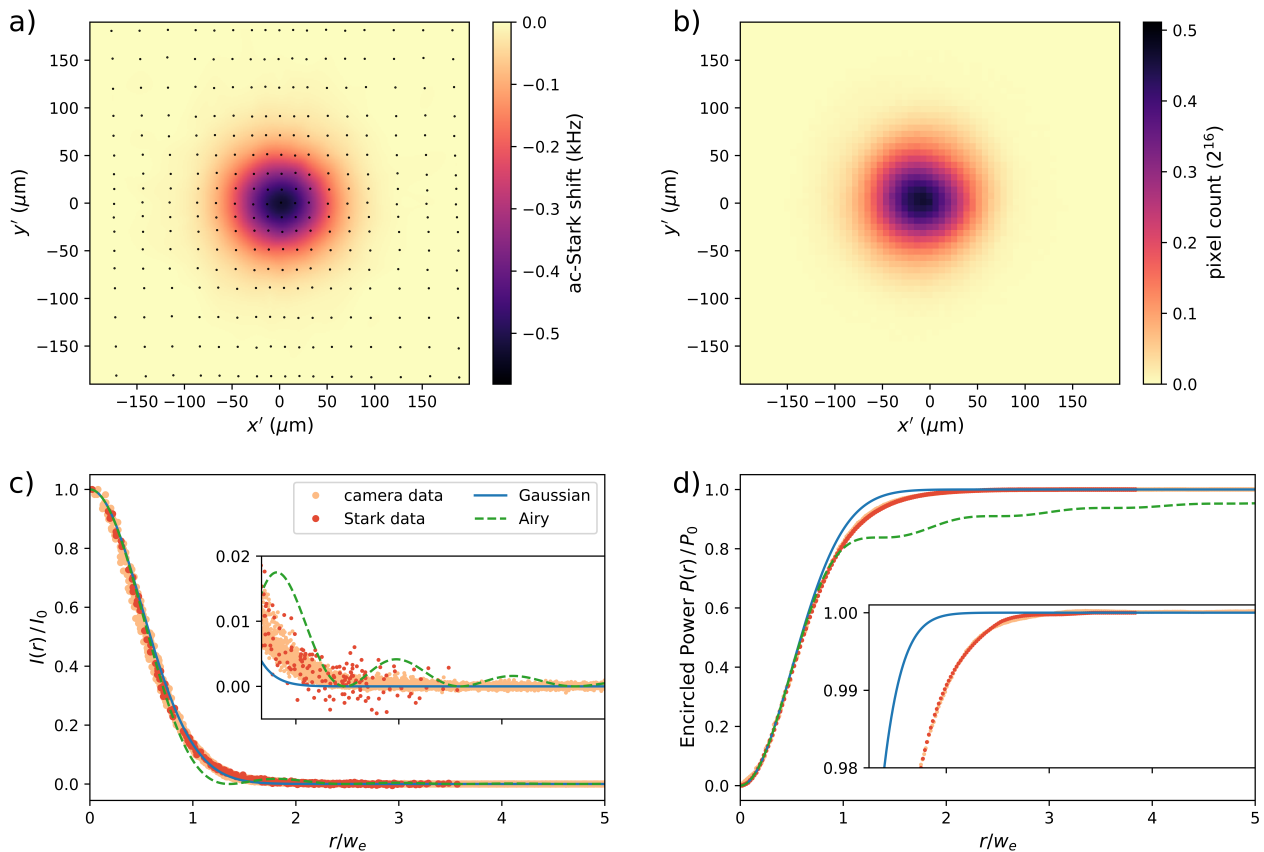


FIG. 3. (Color Online) Beam profiling data for the 598 nm laser. (a) Cubic-spline interpolation to ac-Stark shift measurements. Black points indicate the measurement positions as determined by the CCD camera. (b) Beam profile captured on a low-noise camera outside the chamber at the focal plane of the ion. (c) Measured intensity as a function of radial distance from the beam center for the Stark shift (dark orange) and camera (light orange) data. (d) Fraction of encircled power within radius  $r$ . (c-d) Gaussian (blue solid line) and Airy (green dashed line) test functions with the same normalization  $C$  as the measured profile for comparison. Inset plots show magnified views for clarity.

have a suitable camera to profile this wavelength. For the available camera profiles, Fig. 4 shows  $P_{\text{loss}}$  evaluated as a function the halfwidth,  $l$ , of a square integration region. For those wavelengths with a camera profile,  $P_{\text{loss}}$  is estimated from the corresponding beam profile. For those wavelengths without a camera profile,  $P_{\text{loss}}$  is estimated from the common trend observed in the profiles at the other wavelengths.

The normalization constants determined from the ac-Stark shift profiles at all wavelengths are summarized in Table I. The  $C$  values given in Table I are corrected for the power capture effect and the full size of the correction has been included in the uncertainty budget. For the case of 1560 nm, the CCD camera is not sensitive to this wavelength and therefore it was not possible to monitor the stage movements. Additional uncertainty due to stage positioning was included in the bootstrapping method to assess the uncertainty contribution for this wavelength.

Even though the spatial mode is filtered by an optical fiber and focused with optics that have minimal spherical

TABLE I. Results of beam profiling for all laser wavelengths  $\lambda$ .  $l$  is the half-width of the square grid used for the profile, scaled to the effective beam waist  $w_e$ .  $P_{\text{loss}}$  is the fraction of power estimated to be outside the profile data region.  $C$  is the normalization constant as defined in Eq. (1). Uncertainties are given in parentheses.

$\lambda$ (nm)	$l/w_e$	$P_{\text{loss}}$	$C$ ( $\text{mm}^{-2}$ )	$w_e$ ( $\mu\text{m}$ )
598	2.5	0.2%	116.8 (1.1)	73.83 (35)
646	3.0	0.1%	399.5 (2.7)	39.92 (13)
804	1.7	1.3%	293.9 (2.6)	46.43 (21)
848	1.6	1.6%	268.3 (5.3)	48.7 (5)
987	1.7	1.5%	271.4 (4.8)	48.4 (4)
1560	1.8	1.1%	84.2 (1.2)	87.0 (6)

aberration, fitting to gaussian models was found to be insufficient for determining the peak intensity at the 1% level. For example, if an elliptical gaussian distribution including  $\text{TEM}_{0,0}$ ,  $\text{TEM}_{0,1}$ , and  $\text{TEM}_{1,0}$  modes is used,

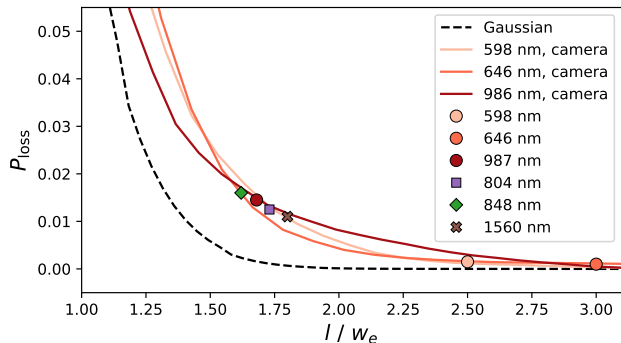


FIG. 4. (Color Online) The fraction of the beam power,  $P_{\text{loss}}$ , not captured in a square region with halfwidth  $l$  scaled to the effective waist  $w_e$ . Solid lines are evaluated from camera beam profiles for the respective wavelengths. For reference, the dashed black line is for a TEM<sub>0,0</sub> Gaussian mode. Points indicate the size of data region used for the respective ac-Stark shift profile scan. For circles,  $P_{\text{loss}}$  is given by the associated camera profile. For others,  $P_{\text{loss}}$  is estimated from the common trend of all the available camera profiles.

as in [6], we found the normalization  $C$  is consistently overestimated by 3-5% for both the ac-Stark shift and camera profile data at all wavelengths compared to the methodology employed here.

### C. Accurate assessment of the 646 and 598 poles

Given the potential to mischaracterize the beam intensity, it would be advantageous to have an independent measurement to validate the methodology. This can be done by conducting measurements near-to-resonant with a contributing transition. For Lu<sup>+</sup>, ideal candidates are the  $^3D_1 \leftrightarrow ^3P_0$  and  $^3D_1 \leftrightarrow ^3P_1$  transitions at 646 and 598 nm, respectively. Sufficiently near to the pole, the polarizability is, to a good approximation, determined by the single pole. Additionally, there can be a measurable scattering rate, which is proportional to the ac Stark shift and the linewidth of the transition. The ratio of ac Stark shift to scattering rate is then independent of the laser intensity. As demonstrated in [4], this can provide an accurate assessment of the corresponding matrix element and hence polarizability.

#### 1. 646 pole via polarizability

The intensity of the Stark shift-inducing laser at 646 nm is actively stabilized with a peak intensity at the ion of  $I_0 = 1.942(21) \text{ Wcm}^{-2}$ , as assessed by the methods of the previous sections. The laser is linearly polarized with the magnetic field aligned to the beam propagation axis ( $\phi = 90^\circ$ ) and detuned by  $\Delta_0/2\pi = -241.7(2) \text{ GHz}$  from the  $|^3D_1, 7, 0\rangle \leftrightarrow |^3P_0, 7, 0\rangle$  transition. All other tran-

sitions combined are estimated to contribute less than  $< 0.2\%$  to the differential dynamic polarizability of the clock transition at this detuning. To a good approximation, the ac Stark shift,  $\hbar\delta_0$ , of the  $|^3D_1, 7, 0\rangle$  state is

$$\delta_0 = \frac{1}{6} \frac{\Omega_0^2}{4\Delta_0} \quad (2)$$

where  $\Omega_0 = \frac{ea_0}{\hbar} \sqrt{\frac{2I_0}{\epsilon_0 c}} \langle ^3D_1 || r || ^3P_0 \rangle$ . The measured shift of  $\delta_0/2\pi = -846.5(3) \text{ Hz}$  at the position of peak intensity yields the matrix element:

$$|\langle ^3D_1 || r || ^3P_0 \rangle| = 1.432(8) \text{ a.u.} \quad (3)$$

#### 2. 646 pole via the scattering rate to stark shift ratio

The 646 laser for this measurement is derived from the detection and cooling laser but frequency offset to a detuning of  $\Delta_0/2\pi \sim -1 \text{ GHz}$  from the  $|^3D_1, 7, 0\rangle \leftrightarrow |^3P_0, 7, 0\rangle$  transition. The optical power is actively stabilized but the absolute intensity at the ion is not accurately determined. The beam propagates in the direction of the magnetic field ( $\phi = 90^\circ$ ) and has circular polarization ( $\sigma^+$  coupling). This polarization ensures that once the atom Raman scatters out of  $|^3D_1, 7, 0\rangle$  it cannot return to this state (Fig. 5a). An atom prepared in the  $|^3D_1, 7, 0\rangle$  state scatters via the  $|^3P_0, 7, +1\rangle$  state at the rate

$$R_0 = \frac{\Gamma_0}{6} \frac{\Omega_0^2}{4\Delta_0^2} \quad (4)$$

where  $\Gamma_0$  is radiative decay rate of the  $^3P_0$  state. From the ratio of Eq. (2) and Eq. (4), one finds

$$\Gamma_0 = \frac{R_0 \Delta_0}{\delta_0} \quad (5)$$

where  $R_0$ ,  $\Delta_0$ , and  $\delta_0$  are all readily measurable quantities without characterization of the laser intensity. Once  $\Gamma_0$  is determined, it is related to the matrix element by:

$$\Gamma_0 = \frac{\omega_0^3 e^2 a_0^2}{3\pi\epsilon_0 \hbar c^3} |\langle ^3D_1 || r || ^3P_0 \rangle|^2, \quad (6)$$

where  $\omega_0$  is the resonant transition frequency.

The experimental procedure to measure  $R_0$  is:

1. Repeat optical pumping into  $|^3D_1, 7, 0\rangle$  ( $\sim 95\%$ ), shelving to  $|^1S_0, 7, -1\rangle$  on the clock transition, and detection of  $^3D_1$  population until the atom is detected dark. This prepares the atom in  $|^1S_0, 7, -1\rangle$  with  $\sim 99.8\%$  fidelity.
2. Shelve  $|^1S_0, 7, -1\rangle$  back to  $|^3D_1, 7, 0\rangle$  with probability  $P_s \approx 0.99$ .
3. Apply detuned 646 laser for duration  $\tau$

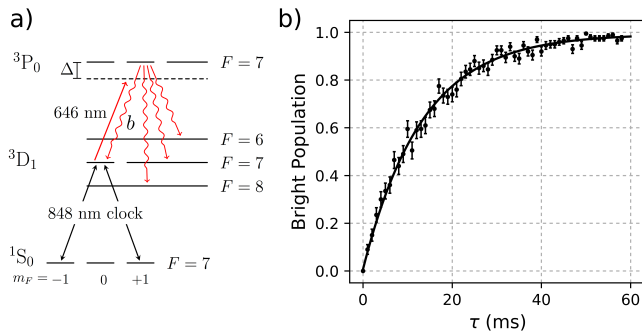


FIG. 5. (Color Online) (a) Schematic of relevant energy levels. Population initially prepared in  $|^3D_1, 7, 0\rangle$  is pumped out by a detuned 646 nm laser with circular polarization. The 848 nm clock laser is used for shelving to measure the population of  $|^3D_1, 7, 0\rangle$  and to measure the ac Stark shift induced by the 646 nm laser. (b) Population pumped out of  $|^3D_1, 7, 0\rangle$  after a 646 nm pulse of duration  $\tau$ . Black line is a fit to Eq. (7).

4. Shelve remaining  $|^3D_1, 7, 0\rangle$  population to  $|^1S_0, 7, +1\rangle$  with probability  $P_s$

5. Detect  $^3D_1$  population

The measured bright population after a pulse length of  $\tau$  is then:

$$p(\tau) = P_s(1 - P_s e^{-R_0(1-b)\tau}), \quad (7)$$

where  $b$  is the fraction of Rayleigh scattering events back to  $|^3D_1, 7, 0\rangle$  and is equal to  $\frac{1}{6}$  for the states considered (Fig. 5a inset).

Fig. 5b shows the result of a typical preliminary experiment run which is fit to Eq. (7) with  $P_s$  and  $R_0$  as free parameters. We acquire statistics on  $P_s$ ,  $R_0$ , and  $\delta_0$  from three interleaved experiments: (i) measure the bright population after preparation but without a 646 pulse to determine  $P_s$  (ii) measure the population after a 646 pulse of fixed duration to determine  $R_0$  from Eq. (7), and (iii) measure the ac-Stark on the  $|^3D_1, 7, 0\rangle$  state using the 848-nm clock transition.

Fig. 6a shows the result from 15 hours of continuous data acquisition, grouped into blocks of 2000 cycles of the interleaved experiments. From the allan deviation of the measured quantities ( $P_s$ ,  $P(\tau)$ , and  $\delta_0$ ), we are able to characterize the stability of systematics such as the shelving probability and laser intensity. The evaluated  $\langle ^3D_1 || r || ^3P_0 \rangle$  is insensitive to slow variation in these systematics and thus the final uncertainty is expected to be statistically limited. Indeed, the Allan deviation (Fig. 6b) indicates the result averages down with projection-noise limited statistics. Fig. 6c shows all results from three consecutive days with a combined measurement time of approximately 35 hours. Black circles were taken at a detuning  $\Delta_0 = 2\pi \times -989.46(10)$  MHz and the black square at  $-1119.46(10)$  MHz.

The weighted mean result of the three experiments is

$$\langle ^3D_1 || r || ^3P_0 \rangle = 1.440(2) \text{ a.u.}, \quad (8)$$

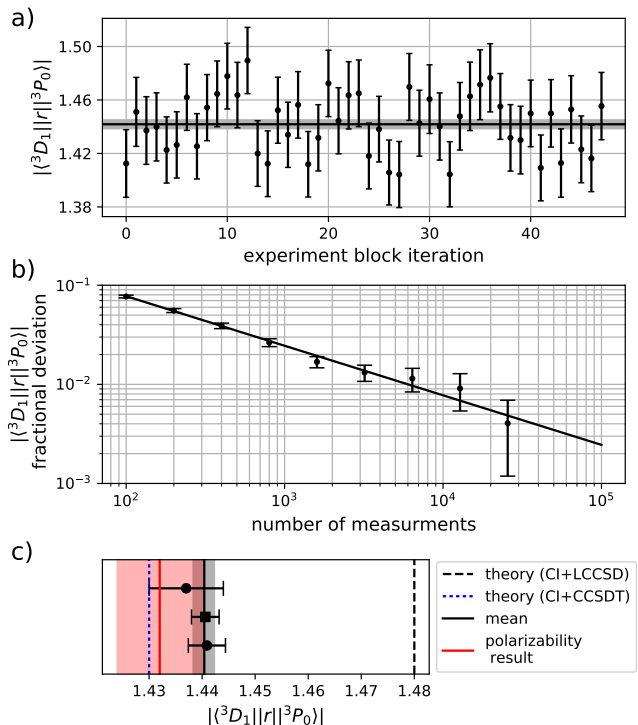


FIG. 6. (Color Online) (a) Each point represents a block of 2000 experiment cycles as describe in the main text. The mean value is 1.441(3) (solid line and shaded region) with reduced  $\chi^2 = 0.82$ . (b) Allan deviation of the dataset in (a) where the solid line is the projection noise limit. (c) Comparison of the matrix element determined from the polarizability method (red line) and the scattering rate to Stark shift ratio (black line) from multiple experimental datasets (black circles/squares). The bottom point (circle) corresponds to the dataset shown in (a)-(b). Shaded regions represent respective uncertainties. The black dashed line is the theory value from previous work [9] and the blue dotted line is a new theory value from the method applied in this work, Sec. ID.

indicated by the black line in Fig. 6c. For comparison, the red line is the result from the polarizability measurement, and the dashed lines are theoretical matrix elements from different methodologies discussed in Sec. ID. The results from the two experimental methodologies agree to within one standard error of the largest uncertainty.

Our initial results from the two methodologies were in significant disagreement. The source of the discrepancy was found to be the contribution of the amplified spontaneous emission (ASE) when using diode laser sources near to a resonance. For the polarizability measurement at  $\Delta_0/2\pi = -241.7(2)$  GHz, we used a diffraction grating to filter the ASE before the optical fiber going to the experiment. This increased the measured Stark shift by 2.9(6)% compared to no filtering and for the same laser intensity at ion. For the scattering rate measurement, a Fabry-Pèrot resonant filter was used to suppress ASE and undesired spurious spectral components from

an AOM which were near resonant.

It is also noted that the implied natural decay rate of  ${}^3P_0$  reported here,  $\Gamma_0/2\pi = 2.447(27)$  MHz, is in disagreement with the measurement reported in Ref. [8], 2.579(17) MHz. In Ref. [8], the linewidth of the transition was extracted from the resonant line profile as a 646-nm laser was stepped through the atomic resonance. It was assumed that the laser linewidth would be dominated by Gaussian technical noise sources and result in a Voigt line shape. This 646-nm laser was recently compared to our spectrally narrow optical frequency comb and found instead to have a nearly Lorentzian power spectral density with full-width-half-maximum (FWHM) of 140 kHz. As the FWHM of two Lorentzians add in convolution, broadening due to 646-nm laser linewidth fully accounts for the discrepancy in the earlier measurement. All measurements reported in this work are in a dispersive regime and are not sensitive to laser linewidths.

### 3. 598 pole via polarizability measurement

The intensity of the ac-Stark shift-inducing laser at 598 nm is actively stabilized with a peak intensity at the ion of  $I_0 = 34.4(6)$  mWcm $^{-2}$ . The laser frequency is referenced to an optical frequency comb and set to a detuning of  $\Delta_1/2\pi = -1097.0(1)$  MHz with respect to the  $|{}^3D_1, 7, 0\rangle \leftrightarrow |{}^3P_1, 6, 0\rangle$  transition. The polarization is linear and aligned parallel to the externally applied magnetic field ( $\phi = 0$ ). The Stark shift,  $\hbar\delta_1$ , on the  $|{}^3D_1, 7, 0\rangle$  state is given by

$$\delta_1 = \frac{\Omega_1^2}{4} \left( \frac{4}{45} \frac{1}{\Delta_1} + \frac{7}{90} \frac{1}{\Delta_1 - \omega_{68}} \right), \quad (9)$$

where  $\omega_{68} = 2\pi \times 52.8322$  GHz is the separation of the  ${}^3P_1$   $F=6$  and  $F=8$  hyperfine levels, and  $\Omega_1 = \frac{ea_0}{\hbar} \sqrt{\frac{2I_0}{\epsilon_0 c}} \langle {}^3D_1 || r || {}^3P_1 \rangle$ . The second term in Eq. (9) is due to coupling from the  $|{}^3D_1, 7, 0\rangle \leftrightarrow |{}^3P_1, 8, 0\rangle$  transition and contributes 1.7% to the total Stark shift. Since the laser is  $\pi$  polarized there is no contribution from the  ${}^3P_1$   $F=7$  level. At the position of peak intensity, we measure a shift of  $\delta_1/2\pi = -1318(1)$  Hz. From Eq. (9) we obtain

$$|\langle {}^3D_1 || r || {}^3P_1 \rangle| = 1.265(11) \text{ a.u.} \quad (10)$$

### 4. 598 pole via scattering rate to stark shift ratio

The 598-nm laser has the same polarization and frequency as used in the polarizability measurement. The laser frequency is sufficiently close to the  $|{}^3D_1, 7\rangle \leftrightarrow |{}^3P_1, 6\rangle$  transition that the scattering through  $|{}^3P_1, 8\rangle$  can be neglected. From the  $|{}^3D_1, 7, 0\rangle$  state, the atom will scatter at the rate

$$R_1 = \Gamma_1 \frac{4}{45} \frac{\Omega_1^2}{4\Delta_1^2}, \quad (11)$$

where  $\Gamma_1$  is the total decay rate of the  ${}^3P_1$  state. From the ratio of Eq. (9) and Eq. (11),  $\Gamma_1$  is determined independent of  $\Omega_1$ .

The experimental procedure to measure  $R_1$  is similar to the 646-nm case:

1. Repeat optical pumping into  $|{}^3D_1, 7, 0\rangle$  and shelving to  $|{}^1S_0, 7, -1\rangle$  on the clock transition until the atom is detected dark.
2. Shelve  $|{}^1S_0, 7, -1\rangle$  back to  $|{}^3D_1, 7, 0\rangle$
3. Apply 598 nm laser for duration  $\tau$
4. Detect remaining  ${}^3D_1$  population.

The population dynamics are slightly complicated compared to the 646-nm case because  ${}^3D_1 \leftrightarrow {}^3P_1$  is an open transition. The possible decay paths from  ${}^3P_1$   $F=6$  are shown in Fig. 7a(inset), where  $\beta$  is the branching ratio from  ${}^3P_1 \rightarrow {}^3D_1$ . Scattering via  $|{}^3P_1, 6, 0\rangle$  redistributes the populations,  $p_6$  ( $p_7$ ) in the  ${}^3D_1$   $F=6$  ( $7$ ) hyperfine manifolds by the following rate equations:

$$\frac{dp_6}{dt} = \frac{3}{7}\beta R_1 p_7 \quad (12)$$

$$\frac{dp_7}{dt} = - \left( 1 - \frac{4}{7} \right) \beta R_1 p_7. \quad (13)$$

Solving for initial conditions  $p_7(0) = P_0$  and  $p_6(0) = 0$ , the bright population,  $p_6 + p_7$ , after a pulse of length  $\tau$  is

$$p(\tau) = P_0 \left[ \frac{3\beta}{7-4\beta} + \frac{7-7\beta}{7-4\beta} e^{-R_1(1-\frac{4}{7}\beta)\tau} \right]. \quad (14)$$

The branching ratio  $\beta$  was measured previously in  ${}^{175}\text{Lu}^+$  and reported to be 0.1862(17) [9]. It has been remeasured in  ${}^{176}\text{Lu}^+$  and the same value was found with comparable uncertainty,  $\beta = 0.1862(13)$ .

The model, Eq. (14), does not account for the fact that population decaying to other magnetic substates in  ${}^3D_1$   $F=7$  will subsequently scatter at different rates. However because the branching ratio back to  $F=7$  is only  $\frac{4}{7}\beta \approx 10\%$  and the relative scattering rates for  $\pi$ -coupling from  $|m| = (0, 1, 2)$  are close, (1.0, 0.98, 0.92), this is not expected to bias  $R_1$  comparable to the reported uncertainty.

An example of the observed bright population after a 598-nm laser pulse of duration  $\tau$  is shown in Fig. 7a. The dashed black line indicates the expected asymptotic bright population,  $\frac{3\beta}{7-4\beta} = 0.08936(16)$ , after the  ${}^3D_1$   $F=7$  hyperfine manifold has been emptied. The solid black line is a fit to Eq. (14) with  $P_0$  and  $R_1$  as free parameters. We acquire statistics on  $P_0$ ,  $R_1$ , and  $\delta_1$ , with three interleaved experiments: (i) measure the bright population after preparation but without the 598-nm pulse to determine  $P_0$  (ii) measure the population after a 598-nm pulse of fixed duration to determine  $R_1$  from Eq. (14), and (iii) measure the ac-Stark on the  $|{}^3D_1, 7, 0\rangle$  state using the 848-nm clock transition. From  $P_0$ ,  $R_1$ ,

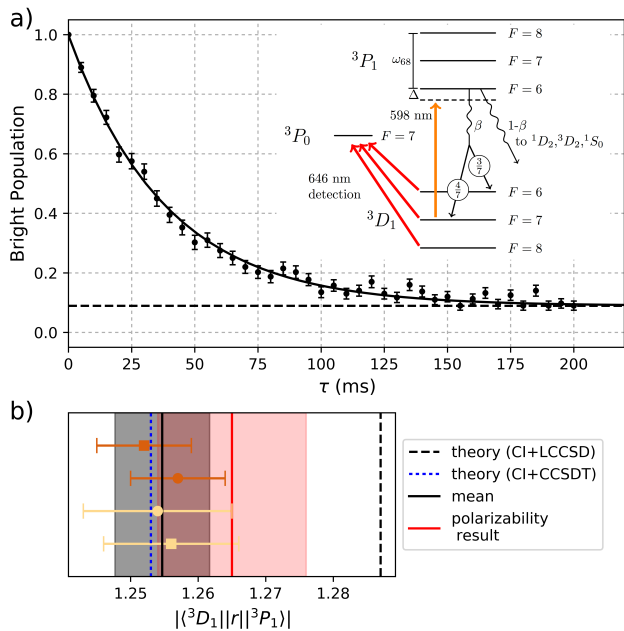


FIG. 7. (Color Online) (a) Bright population remaining after 598-nm laser pulse of duration  $\tau$ . Solid black line is a fit to Eq. (14). a(inset) Schematic of 598-nm scattering experiment including branching paths from the  $^3P_1$   $F=6$  state. (b) Comparison of results from different methodologies. Points are results from scattering to stark shift ratio experiment runs as described in the main text. Light orange points were taken at the detuning of  $-1097.0(1)$  MHz with respect to the  $|^3D_1, 7, 0\rangle \leftrightarrow |^3P_1, 6, 0\rangle$  transition, while dark orange points were at  $+995.7(1)$  MHz with respect to the  $|^3D_1, 7, 0\rangle \leftrightarrow |^3P_1, 8, 0\rangle$  transition. The black line is the  $\chi^2$  optimized mean of these results. Red line is the result from the polarizability measurement. Shaded regions indicate the uncertainties. The black dashed line is the theory value from previous work [9] and the blue dotted line is the new theory value from the method applied in this work, Sec. ID.

and  $\delta_1$  the decay rate  $\Gamma_1$  is found, which is related to the matrix element:

$$\beta\Gamma_1 = \frac{\omega_0^3 e^2 a_0^2}{3\pi\epsilon_0 \hbar c^3} \frac{1}{2J'+1} |\langle ^3D_1 || r || ^3P_1 \rangle|^2, \quad (15)$$

where  $J'$  is the total angular momentum of the excited state.

Fig. 7b shows the results from multiple experiment runs. Light orange points were taken at the detuning of  $-1097.0(1)$  MHz with respect to the  $|^3D_1, 7, 0\rangle \leftrightarrow |^3P_1, 6, 0\rangle$  transition, while dark orange points were at  $+995.7(1)$  MHz with respect to the  $|^3D_1, 7, 0\rangle \leftrightarrow |^3P_1, 8, 0\rangle$  transition. The analysis is modified accordingly for scattering via  $^3P_1$   $F=8$ . Square points used the conditional state preparation step as described, which prepares  $P_0 \approx 99\%$  population in  $|^3D_1, 7, 0\rangle$ . Circles used only 646-nm optical pumping for state preparation which prepares  $\approx 95\%$  of the population in  $|^3D_1, 7, 0\rangle$ , and  $\approx 2\%$  each in  $|^3D_1, 7, \pm 1\rangle$ . From a full rate equa-

TABLE II. Measured peak ac-Stark shifts from which polarizabilities are determined.

$\lambda$ (nm)	$P_0$ (mW)	$\delta f(\phi_m)$ (Hz)	$\delta f_\mu(\phi_m)$ (Hz)	$\delta f_\mu(\pi/2)$ (Hz)
804	12.49 (25)	-316.0 (0.3)	-0.01 (0.26)	168.3 (0.1)
848	16.19 (17)	-286.1 (0.2)	0.13 (0.11)	165.2 (0.1)
987	29.18 (26)	-280.8 (0.4)	-0.07 (0.42)	209.2 (0.1)
1560	441 (10)	-386.0 (0.3)	-0.45 (0.37)	698.4 (0.1)

tion simulation including all magnetic sublevels, we find less than 0.15% deviation of the scattering rate as compared to the model, Eq. (14), for either state preparation method.

The weighted mean result from the four experiment runs is

$$|\langle ^3D_1 || r || ^3P_1 \rangle| = 1.255(7) \text{ a.u.}, \quad (16)$$

indicated by the black line in Fig. 7b. The uncertainty in the mean is limited by the accuracy of  $\beta$ . The polarizability result (red in Fig. 7b) is in agreement to within one standard deviation of the larger uncertainty.

#### D. Polarizability measurement results and comparison with theory

For the remaining wavelengths, the differential dynamic scalar polarizabilities  $\Delta\alpha_0(\omega)$  and tensor polarizabilities  $\alpha_2(^3D_1, \omega)$  of the  $^1S_0 \leftrightarrow ^3D_1$  clock transition are found by the same methodology used in Ref. [2]. The differential ac-Stark shifts induced on the  $|^1S_0, 7, 0\rangle \leftrightarrow |^3D_1, 7, 0\rangle$  optical clock transition,  $\delta f$ , and  $|^3D_1, 6, 0\rangle \leftrightarrow |^3D_1, 7, 0\rangle$  microwave transition,  $\delta f_\mu$ , due to linearly polarized laser light of frequency  $\omega$  are given, in Hz, by [13]

$$\delta f = -\frac{\langle E^2 \rangle}{2\hbar} \left( \Delta\alpha_0(\omega) + \frac{1}{2}\alpha_2(\omega)(3\cos^2\phi - 1) \right) \quad (17)$$

$$\delta f_\mu = -\frac{\langle E^2 \rangle}{2\hbar} \left( \frac{7}{10}\alpha_2(\omega)(3\cos^2\phi - 1) \right) \quad (18)$$

where  $\phi$  is the angle between the laser polarization and quantization axis, and  $\langle E^2 \rangle$  is mean squared electric field averaged over one optical cycle. This is related to the laser intensity by  $\langle E^2 \rangle = I_0/(c\epsilon_0)$ . The peak laser intensity is  $I_0 = CP_0$  where  $P_0$  is the power at the ion and  $C$  is the normalization coefficient found by beam profiling and given in Table I. Polarizabilities are reported in atomic units which can be converted to SI units via  $\alpha/\hbar [\text{Hz m}^2 \text{V}^{-2}] = 2.48832 \times 10^{-8} \alpha$  (a.u.).

To find  $\Delta\alpha_0(\omega)$ , the magnetic field is rotated to  $\phi_m = \cos^{-1}(\sqrt{\frac{1}{3}}) \approx 54.7^\circ$  where the tensor contribution to  $\delta f$  is nulled. The optimal angle is found by measuring  $\delta f_\mu$ . Table II gives measured values of  $\delta f$  and  $\delta f_\mu$  at the optimized angle. The residual Stark shifts measured on the microwave transition imply  $\phi$  has been set to within 1

TABLE III. Measured and calculated differential dynamic scalar polarizabilities  $\Delta\alpha_0(\omega)$  and tensor polarizabilities  $\alpha_2(^3D_1, \omega)$  (in a.u.). The uncertainties are given in parentheses.

$\lambda$ (nm)	Experiment		Theory	
	$\Delta\alpha_0$	$\alpha_2$	$\Delta\alpha_0$	$\alpha_2$
804.13	18.4 (4)	-13.97 (31)	22 (4)	-15.5 (1.2)
847.74	14.06 (31)	-11.59 (26)	17.2 (3.9)	-12.7 (1.0)
987.09	7.56 (15)	-8.05 (16)	9.9 (3.5)	-8.8 (7)
1560.80	2.22 (6)	-5.73 (15)	3.6 (3.1)	-5.9 (5)
10600	0.059 (4) <sup>a</sup>	-4.4 (3) <sup>a</sup>	1.2 (2.9)	-4.9 (4)

<sup>a</sup>These values were obtained in Ref. [2].

mrads of  $\phi_m$  for every wavelength. Uncertainties on all ac Stark shift measurements are statistical from projection noise. To find  $\alpha_2(\omega)$ , the field is rotated to find the extremal Stark shift at  $\phi = \pi/2$ . The measured shifts on the microwave transition at this position are given in Table II. The inferred polarizabilities are summarized in Table III. The measurement wavelengths are given to an accuracy of 0.01 nm in Table III but are known more accurately. A breakdown of the uncertainty budget for  $\Delta\alpha_0(\omega)$  at each wavelength is given in Table IV.

We compare polarizability measurements with theoretical calculations. In Ref. [9], we used a method that combines configuration interaction (CI) and the linearized coupled-cluster single-double (LCCSD) approaches to study  $\text{Lu}^+$ . The application of this method to the calculation of polarizabilities was described in detail. In this work we further develop this method, additionally including quadratic non-linear terms and (partially) triple excitations in the framework of the coupled-cluster approach to improve the effective Hamiltonian used in the CI calculation. The triple excitations are allowed from the core shells with principal quantum numbers  $n = 4, 5$  to the virtual orbitals with maximal quantum numbers  $n = 15$  and  $l = 3$ . Following the formalism developed in [10] we solve equations for triple cluster amplitudes iteratively, i.e., triples are included in all orders of the perturbation theory. The results obtained in the approach combining CI and coupled-cluster single-double-triple (CCSDT) method (we refer to it as the CI+CCSDT method) are listed in Table III. At  $\lambda = 10600$  nm, the theory is unable to provide a reliable prediction because the value is consistent with zero with the theoretical uncertainty. We use the effective (“dressed”) electric dipole operator in the polarizability calculations, which includes the random-phase approximation, core-Brueckner, two particle, structural radiation, and normalization corrections. A detailed description of these corrections is given in Ref. [11]. The assignment of theoretical uncertainties is as discussed in Ref. [9]. As seen from the table, there is a good agreement between theory and experiment, though the experimental accuracy is better.

In Table V we compare the absolute values of the reduced matrix elements  $\langle 5d6s\ ^3D_1 || r || 6s6p\ ^3P_{0,1} \rangle$  obtained

TABLE IV. Contributions to the uncertainty in  $\Delta\alpha_0$  for each wavelength.

effect	804	848	987	1560
	%	%	%	%
beam profiling	0.9	2.0	1.8	1.4
power measurement, statistical	1.8	0.6	0.4	2.3
power meter calibration	0.8	0.8	0.8	0.8
ac Stark shift, statistical	0.06	0.06	0.1	0.03
total uncertainty	2.2	2.2	2.0	2.7

TABLE V. The absolute values of the reduced matrix elements  $\langle 5d6s\ ^3D_1 || r || 6s6p\ ^3P_{0,1} \rangle$  (in a.u.) obtained in the CI+CCSDT method are compared with the results obtained in the CI+LCCSD approximation in Ref. [9] and present experimental results. The uncertainties are given in parentheses.

	Ref. [9]	This work	
	CI+LCCSD	CI+CCSDT	Expt.
$ \langle ^3D_1    r    ^3P_0 \rangle $	1.480	1.430	1.440(2)
$ \langle ^3D_1    r    ^3P_1 \rangle $	1.287	1.253	1.255(7)

in this work with current experimental results and the values obtained in the framework of the CI+LCCSD approximation in Ref. [9]. We find that the inclusion of the non-linear and triple terms into consideration significantly improved the agreement between the theoretical and experimental values.

## II. MODELING THE DIFFERENTIAL POLARIZABILITY

The scalar dynamic polarizability of a given clock state  $|\nu\rangle$  can be written as a positive sum of second order poles. In atomic units, this is given by [12, 13]:

$$\alpha_0(\omega) = \frac{2}{3(2J_\nu + 1)} \sum_{\xi} \frac{\langle \xi || r || \nu \rangle^2}{\omega_{\xi\nu}} \frac{1}{1 - (\omega/\omega_{\xi\nu})^2}, \quad (19)$$

where  $\langle \xi || r || \nu \rangle$  is the reduced dipole matrix element for a transition at frequency  $\omega_{\xi\nu} = E_\xi - E_\nu$ , and  $J_\nu$  is the total angular momentum of state  $|\nu\rangle$ .

Using the identity

$$\frac{1}{1 - x^2} = \frac{x^{2(n+1)}}{1 - x^2} + \sum_{k=0}^n x^{2k} \quad (20)$$

any pole can be split into the sum of a polynomial of order  $2n$  and a term that is henceforth referred to as the pole residual. From calculated matrix elements [9], pole residuals for each contributing transition can be calculated at each measurement wavelength. For  $n = 2$ , these results are tabulated in table VI along with subtotals for each clock state. The two dominant contributions

TABLE VI. The  $n = 2$  residuals for each pole contributing to  $\Delta\alpha_0(\omega)$  evaluated at  $\omega_{804}$  and  $\omega_{848}$ . For the 598- and 646-nm poles, the values are determined from the measured matrix elements. All others are taken from theory [9] using experimental energies. Subtotals given for the  ${}^3D_1$  state omit the two dominant contributions from the 598- and 646-nm poles.

State	Contribution	804-nm	848-nm
$6s^2 {}^1S_0$	$6s6p {}^3P_1^o$	0.029	0.021
	$6s6p {}^1P_1^o$	0.063	0.045
	$5d6p {}^3D_1^o$	9.4[-4]	6.9[-4]
	$5d6p {}^3P_1^o$	1.5[-4]	1.1[-4]
	$5d6p {}^1P_1^o$	4.1[-4]	3.0[-4]
	Total	0.094	0.067
$5d6s {}^3D_1$	$6s6p {}^3P_0^o$	4.990	3.074
	$5d6p {}^3P_0^o$	6.0[-3]	4.4[-3]
	$6s6p {}^3P_1^o$	1.752	1.135
	$5d6p {}^3D_1^o$	0.023	0.017
	$5d6p {}^3P_1^o$	7.3[-3]	5.3[-3]
	$6s6p {}^3P_2^o$	0.022	0.015
	$5d6p {}^3F_2^o$	0.086	0.061
	$5d6p {}^1D_2^o$	0.012	9.0[-3]
	$5d6p {}^3D_2^o$	0.016	0.011
	$5d6p {}^3P_2^o$	4.2[-4]	3.0[-4]
Subtotal	0.174	0.124	

from the 598 and 646-nm transitions are omitted from the  ${}^3D_1$  subtotal. As the residuals are less significant at longer wavelengths, only results for the measurement wavelengths of 804 and 848 nm are given.

As seen from the table, the residual contribution from either clock state is at most the measurement error for any given measurement wavelength and, even then, there is a significant cancellation between them. The omission of these residuals is then well justified even for rather significant changes to the theoretical calculations. Additionally, with 1% accuracy on the contributions from 598 and 646, the error from this is no more than 30% of the measurement error. Hence,  $\Delta\alpha_0(\omega)$  can be modeled by

$$\Delta\alpha_0(\omega) = \frac{2\mu_{598}^2}{9\omega_{598}} \frac{1}{1 - (\omega/\omega_{598})^2} + \frac{2\mu_{646}^2}{9\omega_{646}} \frac{1}{1 - (\omega/\omega_{646})^2} + a_0 + a_1 \left(\frac{\omega}{\omega_{804}}\right)^2 + a_2 \left(\frac{\omega}{\omega_{804}}\right)^4, \quad (21)$$

where  $\mu_\lambda$  are the reduced electric dipole matrix elements for the respective transitions,  $\omega_{646}$  and  $\omega_{598}$  are the respective resonant transition frequencies, and  $a_k$  are polynomial fitting coefficients. The scaling of the frequency for the polynomial terms is arbitrary and conveniently set to the largest frequency in the measurement window,  $\omega_{804}$ . Using Eq. (20) and a suitably modified  $a_k$ , this can

be rewritten in the mathematically equivalent form

$$\Delta\alpha_0 = b_{598}(\omega) + b_{646}(\omega) + \sum_{k=0}^2 a_k \bar{\omega}^{2k}, \quad (22)$$

where  $\bar{\omega} = \omega/\omega_{804}$  and

$$b_\lambda(\omega) = \frac{2\mu_\lambda^2}{9\omega_\lambda} \frac{(\omega/\omega_\lambda)^6}{1 - (\omega/\omega_\lambda)^2}. \quad (23)$$

Values for  $a_k$  can then be found from a  $\chi^2$ -minimization.

As the fitting function is a linear combination of bases functions, the minimization can be elegantly solved using singular-valued decomposition (SVD). The functional form of  $b_\lambda(\omega)$  is practically exact as the transition frequencies are well known [8]. Only the overall scale, which is determined by the relevant matrix element (squared), is subject to experimental uncertainty. For now we assume these are exact. With measurements,  $\mathbf{m}_j$ , of the polarizability performed at  $\omega_j$  with uncertainties  $\sigma_j$ , we seek to find coefficients  $\mathbf{a}$  via the  $\chi^2$ -minimization,

$$\min_{\mathbf{a}} \|\mathbf{A} \cdot \mathbf{a} - \mathbf{b}\|^2 \quad (24)$$

where

$$(\mathbf{A})_{jk} = \frac{\bar{\omega}_j^{2k}}{\sigma_j}, \quad \mathbf{b}_j = \frac{(\mathbf{m} - \mathbf{b}_{598} - \mathbf{b}_{646})_j}{\sigma_j}, \quad (25)$$

and  $(\mathbf{b}_\lambda)_j = b_\lambda(\omega_j)$ . With the SVD,  $\mathbf{A} = \mathbf{U}\mathbf{S}\mathbf{V}^T$ , the solution is then

$$\mathbf{a} = \mathbf{V}\mathbf{S}^{-1}\mathbf{U}^T\mathbf{b}, \quad (26)$$

where  $\mathbf{S}^{-1}$  is to be interpreted as the left inverse. The polarizability at any given frequency is then given by

$$\Delta\alpha_0(\omega) = \mathbf{a} \cdot \mathbf{v}(\bar{\omega}) + b_{598}(\omega) + b_{646}(\omega) \quad (27)$$

with  $\mathbf{v}(x) = (1, x^2, x^4)$ .

In terms of errors there are two distinct considerations. The first is simply the error associated with the fit, which arises from the first term in the equation for  $\alpha_0(\omega)$ . As this is a linear combination of the coefficients  $\mathbf{a}$ , the 1- $\sigma$  error is given by

$$\delta\alpha_0(\omega) = \sqrt{\mathbf{v}(\bar{\omega})^T (\mathbf{A}^T \mathbf{A})^{-1} \mathbf{v}(\bar{\omega})}, \quad (28)$$

which cannot be treated as uncertainties in each of the polynomial coefficients. Although each coefficient  $a_k$  can be prescribed an uncertainty, each of these uncertainties has some degree of correlation which is accounted for by Eq. 28 insofar as the evaluation of the polarizability at a given frequency is concerned.

The second consideration is from an error in  $b_\lambda(\omega)$ . Varying either of these by the fractional amount  $\sigma_\lambda$  will change the solution by

$$\delta\alpha_0(\omega) = - \left( \mathbf{v}(\bar{\omega})^T \mathbf{V}\mathbf{S}^{-1}\mathbf{U}^T \left( \frac{\mathbf{b}_\lambda}{\sigma} \right) \right) \sigma_\lambda + b_\lambda(\omega)\sigma_\lambda, \quad (29)$$

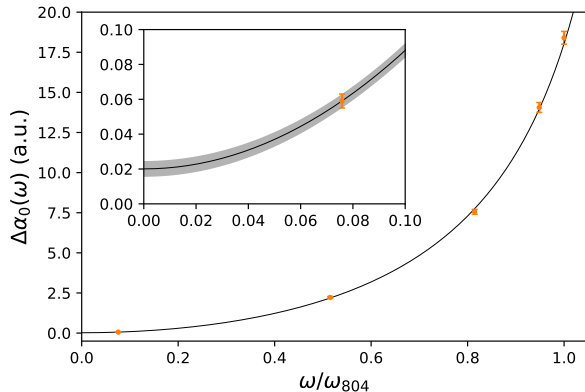


FIG. 8. (Color Online) Polarizability measurement results (orange points) from Table III and fit to the model given by Eq. (27) (solid black line). The inset shows the model uncertainty (gray shaded) near dc, which is predominately determined by the measurement uncertainty at  $10.6 \mu\text{m}$  (orange point inset).

where  $\boldsymbol{\sigma}$  is the vector of measurement uncertainties,  $\sigma_j$ , and the vector division is to be interpreted element-wise. As  $\mathbf{v}$  and  $\mathbf{A}$  are unaffected, the error given by Eq. 28 is unchanged. Note that both  $\sigma_{598}$  and  $\sigma_{646}$  are  $\lesssim 0.01$ . As it turns out, these errors are much smaller than those from the fit and can be largely ignored being no more than around 5% of the fitting error over the frequency range of interest. The reason for this is that small changes in  $b_\lambda(\omega)$ , that may make significant changes to the polarizability, are largely compensated by the fitting so as to remain consistent with the measurements.

The result of the minimization procedure described above is shown in Fig. 8. We find

$$\Delta\alpha_0(0) = 0.0201(45) \quad (30)$$

with a reduced  $\chi^2 = 1.48$ . The extrapolated value is consistent with that determined from the measurement at  $10.6 \mu\text{m}$  and extrapolated using theory [2]. The error bar also reflects the intuitively obvious fact that the error in the extrapolation cannot be better than the measurement error at  $10.6 \mu\text{m}$ : with a three parameter fit to five data points there is insufficient averaging to expect better particularly with the other measurements far removed from the extrapolation point. This should be contrasted with the claim in [6].

It is of interest to compare and contrast the model used with the single pole approximation [6]

$$\Delta\alpha_0(\omega) \approx c_0 + \frac{c_1(\omega/\omega_0)^2}{1 - (\omega/\omega_0)^2}, \quad (31)$$

which may be viewed as a Padé approximant accurate to 4<sup>th</sup> order. In general, care should be taken with such an approximation: it constrains the relative signs of the

quadratic and quartic terms and this need not be the case for a differential polarizability in which there can be significant pole cancellation. In the case of lutetium,  $\Delta\alpha_0(\omega)$  is dominated by two transitions connected to  $^3D_1$  which ensures the relative sign. Moreover the two poles are closely spaced and reasonably removed from the measurement window of interest. Hence such an approximation may be reasonable. Fitting to this model gives  $\Delta\alpha_0(0) = 0.0203(42)$  with a reduced  $\chi^2$  of 0.94, in complete agreement with the previous fit. Additionally, the effective pole at  $\omega_0$  has a wavelength of  $639(7) \text{ nm}$  consistent with the expectation that it lies between the two dominant poles at  $598$  and  $646 \text{ nm}$  and weighted towards the strongest contribution at  $646 \text{ nm}$ . As there is no significant modeling dependence, we use the more general model in assessing the BBR shift for the convenience that comes with the linear parameter dependence.

### III. THE BBR SHIFT ASSESSMENT

With  $\Delta\alpha_0(\omega)$  experimentally characterized up to  $\omega_{804}$ , the BBR shift can be readily calculated. Integrating over the BBR spectrum we have

$$\delta\nu = -\frac{1}{2} \int_0^\infty \Delta\alpha_0(\nu) \frac{8\pi h}{c^3 \epsilon_0} \frac{\nu^3}{e^{h\nu/(k_B T)} - 1} d\nu \quad (32)$$

$$= -\frac{1}{2} \left( \frac{8\pi^5 k_B^4 T_0^4}{15 h^3 c^3 \epsilon_0} \right) \left( \frac{T}{T_0} \right)^4 \times \frac{15}{\pi^4} \int_0^\infty \Delta\alpha_0(u) \frac{u^3}{e^u - 1} du \quad (33)$$

$$= -\frac{1}{2} (831.945 \text{ V/m})^2 \left( \frac{T}{T_0} \right)^4 \times \frac{15}{\pi^4} \int_0^\infty \Delta\alpha_0(u) \frac{u^3}{e^u - 1} du, \quad (34)$$

where  $T_0 = 300 \text{ K}$  and  $u = h\nu/(k_B T)$  is a dimensionless scale of integration. Defining  $\bar{T} = T/T_0$  and using Eq. 27, the BBR shift can be written

$$\delta\nu = -\frac{1}{2} (831.945 \text{ V/m})^2 \bar{T}^4 \mathbf{a} \cdot \mathbf{w}(\bar{T}), \quad (35)$$

where

$$\mathbf{w}(\bar{T}) = \left( 1, \frac{40\pi^2}{21} \epsilon^2 \bar{T}^2, 8\pi^4 \epsilon^4 \bar{T}^4 \right), \quad \epsilon = \frac{k_B T_0}{\hbar \omega_{804}}. \quad (36)$$

From the fitted coefficients, the fractional BBR shift is then given by

$$\frac{\delta\nu}{\nu} = -4.90 \times 10^{-19} \bar{T}^4 (1 + 1.77 \bar{T}^2), \quad (37)$$

where the term proportional to  $\bar{T}^8$  has been omitted as it contributes only  $\sim 1\%$  at  $300 \text{ K}$ .

As with the polarizability itself, only the fitting error significantly influences the uncertainty. Also, although

the BBR shift is best given as an expansion of varying powers of temperature, the uncertainty in its estimate is best represented by a term similar to Eq. 28 and not independent uncertainties of the expansion coefficients. Explicitly

$$2.45 \times 10^{-17} \bar{T}^4 \sqrt{\mathbf{w}(\bar{T})^T (\mathbf{A}^T \mathbf{A})^{-1} \mathbf{w}(\bar{T})}, \quad (38)$$

and, over the practical temperature range of 270-330 K, this is well approximated by  $9.8 \times 10^{-20} \bar{T}^4$ . Corrections due to Eq. 29 are less than 1% of this expression. The BBR shift at room temperature is then  $-1.364(98) \times 10^{-18}$  in agreement with the previous assessment [2].

#### IV. CONCLUSION

In summary, the differential polarizability of the  $^{176}\text{Lu}^+ \ ^1S_0 \leftrightarrow \ ^3D_1$  clock transition has been measured over a range of wavelengths. This has allowed an extrapolation to the true static value relevant to micromotion clock shifts and an experimental determination of the dynamic correction to the BBR shift. Model dependency for the extrapolation was investigated using two independent fitting models: both of which could be justified based on theoretical considerations and gave excellent agreement in the extrapolated value.

The experimental determination of intensities is a crucial component of the polarizability assessment and this was rigorously tested using an independent polarizability measurement near to resonance with two contributing transitions. We consider this an essential consistency check when using extrapolation of high accuracy polarizability measurements for BBR shift assessments. Such a consistency check is readily available for any clock candidate having a transition associated with detection. The measurements also provided precision benchmarks for the theoretical approach developed in this work.

#### V. ACKNOWLEDGEMENTS

This work is supported by the National Research Foundation, Prime Ministers Office, Singapore and the Ministry of Education, Singapore under the Research Centres of Excellence programme. It is also supported by A\*STAR SERC 2015 Public Sector Research Funding (PSF) Grant (SERC Project No: 1521200080). T. R. Tan acknowledges support from the Lee Kuan Yew post-doctoral fellowship. This work was supported in part by the Office of Naval Research, USA, under award number N00014-17-1-2252 and Russian Foundation for Basic Research under Grant No. 17-02-00216.

- 
- [1] M. S. Safronova, D. Jiang, B. Arora, C. W. Clark, M. G. Kozlov, U. I. Safronova, and W. R. Johnson, *IEEE transactions on ultrasonics, ferroelectrics, and frequency control* **57** (2010).
  - [2] K. Arnold, R. Kaewuam, A. Roy, T. Tan, and M. Barrett, *Nature Communications* **9** (2018).
  - [3] P. Dubé, A. A. Madej, M. Tibbo, and J. E. Bernard, *Phys. Rev. Lett.* **112**, 173002 (2014).
  - [4] M. Hettrich, T. Ruster, H. Kaufmann, C. Roos, C. Schmiegelow, F. Schmidt-Kaler, and U. Poschinger, *Phys. Rev. Lett.* **115**, 143003 (2015).
  - [5] T. Rosenband, W. M. Itano, P. Schmidt, D. Hume, J. Koelemeij, J. C. Bergquist, and D. J. Wineland, in *Frequency and Time Forum (EFTF), 2006 20th European* (IEEE, 2006) pp. 289–292.
  - [6] N. Huntemann, C. Sanner, B. Lipphardt, C. Tamm, and E. Peik, *Phys. Rev. Lett.* **116**, 063001 (2016).
  - [7] C. Tamm, S. Weyers, B. Lipphardt, and E. Peik, *Phys. Rev. A* **80**, 043403 (2009).
  - [8] R. Kaewuam, A. Roy, T. R. Tan, K. J. Arnold, and M. D. Barrett, *Journal of Modern Optics* **65**, 592 (2018).
  - [9] E. Paez, K. J. Arnold, E. Hajiyev, S. G. Porsev, V. A. Dzuba, U. I. Safronova, M. S. Safronova, and M. D. Barrett, *Phys. Rev. A* **93**, 042112 (2016).
  - [10] S. G. Porsev and A. Derevianko, *Phys. Rev. A* **73**, 012501 (2006).
  - [11] V. A. Dzuba, M. G. Kozlov, S. G. Porsev, and V. V. Flambaum, *Zh. Eksp. Teor. Fiz.* **114**, 1636 (1998), [*Sov. Phys.-JETP* **87** 885, (1998)].
  - [12] B. Arora, M. Safronova, and C. W. Clark, *Phys. Rev. A* **76**, 052509 (2007).
  - [13] F. Le Kien, P. Schneeweiss, and A. Rauschenbeutel, *Eur. Phys. J. D* **67**, 92 (2013).